

# In Vivo Measurement of the Brain and Skull Resistivities Using an EIT-Based Method and Realistic Models for the Head

Sónia I. Gonçalves\*, Jan C. de Munck, Jeroen P. A. Verbunt, Fetsje Bijma, Rob M. Heethaar, and Fernando Lopes da Silva

**Abstract**—*In vivo* measurements of equivalent resistivities of skull ( $\rho_{\text{skull}}$ ) and brain ( $\rho_{\text{brain}}$ ) are performed for six subjects using an electric impedance tomography (EIT)-based method and realistic models for the head.

The classical boundary element method (BEM) formulation for EIT is very time consuming. However, the application of the Sherman–Morrison formula reduces the computation time by a factor of 5. Using an optimal point distribution in the BEM model to optimize its accuracy, decreasing systematic errors of numerical origin, is important because cost functions are shallow. Results demonstrate that  $\rho_{\text{skull}}/\rho_{\text{brain}}$  is more likely to be within 20 and 50 rather than equal to the commonly accepted value of 80. The variation in  $\rho_{\text{brain}}$  (average =  $301 \Omega \cdot \text{cm}$ , SD = 13%) and  $\rho_{\text{skull}}$  (average =  $12230 \Omega \cdot \text{cm}$ , SD = 18%) is decreased by half, when compared with the results using the sphere model, showing that the correction for geometry errors is essential to obtain realistic estimations. However, a factor of 2.4 may still exist between values of  $\rho_{\text{skull}}/\rho_{\text{brain}}$  corresponding to different subjects. Earlier results show the necessity of calibrating  $\rho_{\text{brain}}$  and  $\rho_{\text{skull}}$  by measuring them *in vivo* for each subject, in order to decrease errors associated with the electroencephalogram inverse problem. We show that the proposed method is suited to this goal.

**Index Terms**—Electric impedance tomography (EIT), electrical resistivities, electroencephalogram inverse problem (EEG IP), realistic models.

## I. INTRODUCTION

THE INVERSE problem (IP) of electroencephalogram (EEG) aims to determine the sources inside the brain that best explain the electrical potentials measured on the surface of the scalp [4]. The determination of the sources is made through the use of mathematical models ([5]–[8]) which describe the head as an electrical conductor. In this way, the knowledge of the electrical resistivities of the tissues of the

head must be known *a priori*, and it is known that the solution to the EEG IP is highly dependent on the values taken for these parameters ([9]–[15]). The first attempts to measure the electrical resistivities of the tissues [16] were made *in vitro* and often using samples taken from animals. These experiments presented several pitfalls. The tissues were taken from their natural environment and it is known that the death of the tissue induces changes in its electrical properties. On the other hand, values obtained from animal tissues are by no means sufficient since it is known that even within the human tissues the variability of the electrical resistivities is high. In fact, the tissues are inhomogeneous and anisotropic and, therefore, differences in the measured resistivity accompanying variations in the orientation of the cells in the tissue are to be expected. This is the case in, e.g., brain tissue in which the measured resistivity is different if transversal or longitudinal fibers are considered. Also, the resistivity of the tissues depends on factors such as the water content, which might generate a change in the resistivity during measurement. Physiological processes might also induce changes in the electrical resistivity of tissues. Finally, true intersubject variations [2] in the measured conductivity are to be expected due to the natural variation of the tissues from individual to individual. As a consequence, the values presented in literature for the electrical resistivities show a wide range of variation and there might be a factor of 7 between the minimum and maximum resistivity values reported for a certain tissue [17]. In the past years, several studies have been performed to try to estimate *in vivo* the electrical resistivities of the head tissues ([18]–[21]). In particular, Oostendorp *et al.* [18] used the boundary element method (BEM) to estimate the equivalent electrical resistivities of brain, skull, and scalp. However, since the numerical accuracy of the BEM is highly dependent on the skull-to-brain resistivity ratio, as well as on the way the nodes are distributed among the several compartments [22], the use of BEM is susceptible to introduce systematic errors in the estimation of this ratio. Furthermore, this accuracy dependence, which was not considered in previous studies, is different for EEG and for electric impedance tomography (EIT).

In the present work, *in vivo* measurements of the electrical resistivities of brain ( $\rho_{\text{brain}}$ ), skull ( $\rho_{\text{skull}}$ ), and scalp ( $\rho_{\text{scalp}}$ ) are performed for six different subjects, using the approaches described in ([2] and [3]). However, different from [2], realistic models, instead of spherical models, are used to describe the head and the BEM is used to solve the forward problem of EIT. In order to avoid biased estimations of the electrical resistivities, a thorough study is performed to determine the optimal

Manuscript received March 14, 2002; revised December 8, 2002. The work of S. I. Gonçalves was supported by the Portuguese Foundation for Science and Technology under Ph.D. scholarship Praxis XXI/BD/15502/96. *Asterisk indicates corresponding author.*

\*S. I. Gonçalves is with the MEG Centre—VU University Medical Centre, P.O. Box 7057, 1007 MB Amsterdam, The Netherlands and also with the Faculty of Sciences, Institute of Biophysics and Biomedical Engineering, University of Lisbon, 1700 Campo Grande, Lisbon, Portugal (e-mail: s.goncalves@vumc.nl).

J. C. de Munck, J. P. A. Verbunt, and F. Bijma are with the MEG Centre—VU University Medical Centre, 1007 MB Amsterdam, The Netherlands.

R. M. Heethaar is with the Department of Physics and Medical Technology, Institute of Cardiovascular Research ICaR-VU, VU University Hospital, 1007 MB Amsterdam, The Netherlands.

F. Lopes da Silva is with the Institute of Neurobiology, 1098 SM Amsterdam, The Netherlands.

Digital Object Identifier 10.1109/TBME.2003.812164

conditions yielding the lowest possible BEM numerical error for EIT. Furthermore, the mathematical problem of using the BEM for many combinations of electrical resistivities, although using the same geometry is analyzed and optimized using the Sherman–Morrison–Woodbury formula.

## II. METHODS

### A. The EIT Method

The application of the EIT method to compute equivalent electrical resistivities using spherical models for the head has already been demonstrated in [2] and [3]. In this paper, the same method is applied using realistic models for the head. However, when dealing with the IP of EIT, the adjustment of the conductivities in each iterative step implies that the system matrix must be recomputed, contrary to what happens in the case of the EEG IP where only the right-hand side varies. In computational terms, this becomes extremely time consuming. To overcome this problem, the Sherman–Morrison–Woodbury formula [23] is used to avoid the bulk recomputation of the system matrix in each iterative step.

1) *The Forward Problem Calculation Using BEM*: In the BEM formulation [5], [7], [24], [25], the volume conductor is described by a set of homogeneous, isotropic, and nonintersecting compartments of arbitrary shape, each one characterized by a certain electrical conductivity. It is considered that there are no sources inside the volume and the electrical current enters or leaves the conductor only through electrodes placed on the outer surface. In this study, the volume conductor consists of three nested compartments representing, from outer to inner compartment, scalp, skull, and brain [see Fig. 1(a)]. In this case, the potential generated on a certain point  $\vec{r}_p$  on the surface of the conductor by an injected current density  $\vec{J}(\vec{r}')$  will be given by the integral equation [26]

$$\sigma_p \Psi(\vec{r}_p) = \frac{1}{4\pi} \sum_{i=0}^2 (\sigma_i^- - \sigma_i^+) \oint_{S_i} \Psi(\vec{r}') d\omega_i - \frac{1}{4\pi} \oint_{S_0} \frac{\vec{J}(\vec{r}') \cdot \vec{n}_0}{|\vec{r} - \vec{r}_p|} dS \quad (1)$$

where

- $\sigma_p$  is the conductivity of the outer compartment;
- $\sigma_i^-$  is the inner conductivity of compartment  $i$ ;
- $\sigma_i^+$  is the outer conductivity of compartment  $i$ ;
- $S_i$  is the surface delimiting compartment  $i$ ;
- $\vec{n}_0$  is the normal to surface  $S_0$ ;
- $d\omega_i$  is the solid angle of the elemental surface  $dS_i$  as seen from  $\vec{r}_p$ .

Furthermore, the BEM approach assumes the discretization of the surfaces into a set of triangles whose vertices are the nodes of the surface. When the potential is linearly interpolated over triangles, the potential measured on a certain node  $\mathbf{i}$  of surface  $S_m$  is written as

$$\sigma_m \Psi_i^m = \frac{1}{4\pi} \sum_{k=0}^2 \sum_{j=0}^{N_k-1} (\sigma_k^- - \sigma_k^+) \Omega_{ij}^{mk} \Psi_j^k - \frac{1}{4\pi} (\Gamma_{i1} J_{N,1} - \Gamma_{i2} J_{N,2}) \quad (2)$$

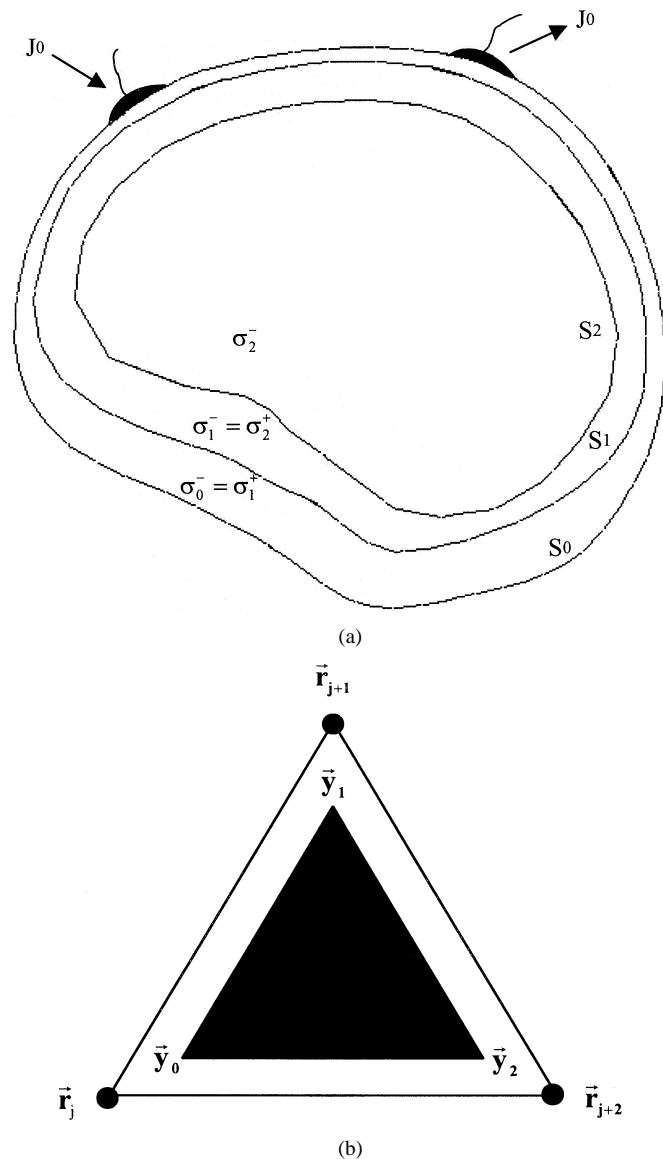


Fig. 1. (a) Schematic representation of the volume conductor used in the BEM formulation for EIT. It is composed of three isotropic and homogeneous compartments representing, respectively, from the outside to the inside, scalp ( $S_0$ ), skull ( $S_1$ ), and brain ( $S_2$ ). Each compartment is characterized by an inner ( $\sigma^-$ ) and outer ( $\sigma^+$ ) conductivity. Current  $J_0$  is injected and extracted on surface electrodes. (b) Schematic representation of the procedure used for the computation of the current density. Given a triangle defined by vertices  $\vec{r}_j$ ,  $\vec{r}_{j+1}$ , and  $\vec{r}_{j+2}$ , the current density is obtained from the computation of the area correspondent to a shrunken version (black triangle) of the original triangle defined by vertices  $\vec{y}_0$ ,  $\vec{y}_1$ , and  $\vec{y}_2$ .

where

- $N_k$  is the number of nodes of surface  $k$ ;
- $\Omega_{ij}^{mk}$  is the linearly weighted solid angle viewed from  $\vec{r}_i$  on surface  $m$ , of the direct neighboring triangles of point  $\vec{r}_j$  on surface  $k$  [5];

$\Gamma_{i1}$  and  $\Gamma_{i2}$  are the integrals of  $(1/|\vec{r} - \vec{r}_p|)$  over the surface element  $dS_0$ , respectively, associated to injection electrode 1 and 2. It is defined according to [5] as (3) (shown at bottom of the next page) where  $\vec{y}_0$ ,  $\vec{y}_1$ , and  $\vec{y}_2$  are the corners of the injection electrode [see Fig. 1(b)] with respect to the view point  $\vec{x}_i$ ,  $\Omega_i$  is the solid angle seen from

point  $i$  with respect to the injection electrode, and the integrals  $\gamma_k^0$  are defined in [5];  
 $\mathbf{J}_{n,j} = (\mathbf{J} \cdot \mathbf{n}_0)_j$  is the current density at triangle  $j$  of surface  $S_0$  where  $j = 1, 2$ . The original triangle is shrunk by a factor of 0.9 and the current density is calculated over the area of the new triangle [see Fig. 1(b)] to avoid singularity problems on (3) when the view point is coincident with one of the three corners.

After some manipulations, (2) can be written in matrix form as

$$\mathbf{A}\Psi = \Gamma\mathbf{J} \quad (4)$$

where

$\mathbf{A}$  is the  $N \times N$  system matrix containing the equation dependence on the electrical conductivities.  $N$  is the total number of nodes of the three surfaces and each matrix element is defined as

$$\mathbf{A}_{ij}^{mk} = \sigma_m \delta_{ij}^{mk} - \frac{1}{4\pi} (\sigma_k^- - \sigma_k^+) \Omega_{ij}^{mk} \quad (5)$$

$\Psi$  is the  $N \times 1$  column vector containing the potential values;

$\Gamma$  is the  $N \times 2$  matrix containing the integrals  $\Gamma_{ij}$ , where  $j = 1, 2$ ;

$\mathbf{J}$  is the  $2 \times 1$  column vector containing the current density values.

Since the solution of (4) is determined up to an arbitrary constant, the system matrix  $\mathbf{A}$  has to be deflated to obtain uniqueness. In this paper, the deflated matrix  $\mathbf{M}$  is defined as

$$\mathbf{M} = \mathbf{A} + \frac{\mathbf{e}\mathbf{e}^T}{N} \quad (6)$$

where  $\mathbf{e}$  is an  $N \times 1$  vector defined as

$$\mathbf{e} = \left[ \begin{array}{c} 1 \\ 1 \\ 1 \\ \vdots \\ 1 \end{array} \right] \Bigg\} N. \quad (7)$$

2) *The IP Calculation Using BEM:* The IP of EIT is solved through the minimization of the cost function defined in [3] and assuming, as in previous studies ([2], [3], [18]), that  $\sigma_{\text{brain}} = \sigma_{\text{scalp}}$

$$\text{Cost} \left( \sigma_{\text{brain}}, \frac{\sigma_{\text{skull}}}{\sigma_{\text{brain}}} \right) = \frac{\sum_{k,i} (\Psi_{ik} - \tilde{\Psi}_{ik})^2}{\sum_{k,i} (\Psi_{ik})^2} \quad (8)$$

where

$i$  runs over the number of measuring electrode pairs;  
 $k$  runs over the number of injection electrode pairs;  
 $\Psi_{ik}$  is the potential measured by electrode pair  $i$  and generated by injection electrode pair  $k$ ;

$\tilde{\Psi}_{ik}$  is the potential predicted on measuring electrode pair  $i$  and generated by injection electrode pair  $k$ .

The forward problem of EIT must be solved in order to obtain the model potential  $\tilde{\Psi}_{ik}$ . This is accomplished through the solution of (4) in order to find  $\Psi$ . However, the adjustment of the electrical conductivities implies the recomputation of the system matrix  $\mathbf{A}$  and the solution of (4) for each one of the iterations, which increases enormously the computational burden. In order to simplify this task, attention was focused on the simplification of matrix  $\mathbf{A}$ , containing the dependence on the electrical conductivities. It can be shown (see Appendix A), making use of matrices (A.2)–(A.10) and the identities in (A.13), that the system matrix  $\mathbf{A}$  can be written as

$$\mathbf{A} = \tilde{\mathbf{A}}\mathbf{\Lambda}_1 + \mathbf{\Lambda}_2 \quad (9)$$

where

$\tilde{\mathbf{A}}$  is the system matrix with  $\sigma_0$  and the conductivity differences set to unity;

$\mathbf{\Lambda}_1$  is the  $N \times N$  diagonal matrix defined as

$$\mathbf{\Lambda}_1 = \text{diag}(-\sigma_0, \dots, -\sigma_0, (\sigma_0 - \sigma_1), \dots, (\sigma_0 - \sigma_1) \\ (\sigma_1 - \sigma_2), \dots, (\sigma_1 - \sigma_2)) \quad (10)$$

where  $N = N_0 + N_1 + N_2$  and each constant is, respectively, repeated  $N_0$ ,  $N_1$ , and  $N_2$  times;

$\mathbf{\Lambda}_2$  is the  $N \times N$  diagonal matrix defined as

$$\mathbf{\Lambda}_2 = \text{diag}(0, \dots, 0, (2\sigma_0 - \sigma_1), \dots, (2\sigma_0 - \sigma_1) \\ (3\sigma_1 - 2\sigma_2), \dots, (3\sigma_1 - 2\sigma_2)) \quad (11)$$

where each constant is, respectively, repeated  $N_0$ ,  $N_1$ , and  $N_2$  times.

The constants  $N_0$ ,  $N_1$ , and  $N_2$  are the number of nodes of surfaces  $S_0$ ,  $S_1$ , and  $S_2$ , corresponding to scalp, skull, and brain and their sum equals the total number of nodes  $N$ . The parameters  $\sigma_0$ ,  $\sigma_1$ , and  $\sigma_2$  are, respectively, the inner conductivities of scalp, skull, and brain.

The decomposition of matrix  $\mathbf{A}$ , as presented in (9), allows the optimization of the computation of  $\Psi$  since the geometrical integrals are stored in memory, thus being computed only once. Furthermore, the Sherman–Morrison–Woodbury formula can be applied to (9) as follows. In the case that the solution  $\Psi$  of a general system of equations  $\mathbf{M}\Psi = \mathbf{b}$  has already been found, then the solution to the new system of equations  $\mathbf{M}'\Psi' = \mathbf{b}$  is found through the application of the Sherman–Morrison–Woodbury formula if  $\mathbf{M}'$  can be written as

$$\mathbf{M}' = \mathbf{M} + \sum_{i=0}^{L-1} \mathbf{u}_i \mathbf{v}_i^T \quad (12)$$

where

$\mathbf{u}_i$  and  $\mathbf{v}_i$  are arbitrary column vectors containing the changes to matrix  $\mathbf{M}$ ;

$L$  is the rank of the update matrix of  $\mathbf{A}$ ;

$\mathbf{M}$  and  $\mathbf{M}'$  are invertible matrices.

$$\Gamma_i = \frac{-\vec{\mathbf{y}}_0 \cdot (\vec{\mathbf{y}}_1 \times \vec{\mathbf{y}}_2) \Omega_i + (\vec{\mathbf{y}}_0 \times \vec{\mathbf{y}}_1 + \vec{\mathbf{y}}_1 \times \vec{\mathbf{y}}_2 + \vec{\mathbf{y}}_2 \times \vec{\mathbf{y}}_0) \cdot \sum_{k=0}^2 (\vec{\mathbf{y}}_k \times \vec{\mathbf{y}}_{k+1}) \gamma_k^0}{|\vec{\mathbf{y}}_0 \times \vec{\mathbf{y}}_1 + \vec{\mathbf{y}}_1 \times \vec{\mathbf{y}}_2 + \vec{\mathbf{y}}_2 \times \vec{\mathbf{y}}_0|} \quad (3)$$

The solution of the disturbed system of equations  $\Psi'$  is found from the original solution  $\Psi$  through the formula [23]

$$\Psi' = \Psi - \mathbf{Z} \cdot \mathbf{x}' \quad (13)$$

where

$\mathbf{Z}$  is an  $N \times L$  matrix, the columns of which are vectors  $\mathbf{z}_i$ , defined as the solutions to the set of equations

$$\mathbf{M}\mathbf{z}_i = \mathbf{u}_i \quad (14)$$

where  $i$  ranges from 0 to  $L - 1$ ;

$\mathbf{x}'$  is the solution to the system of equations

$$\mathbf{B}\mathbf{x}' = \mathbf{V}^T \Psi \quad (15)$$

given that

$\mathbf{B}$  is an  $L \times L$  matrix defined as

$$\mathbf{B} = \mathbf{1} + \mathbf{V}^T \mathbf{Z} \quad (16)$$

$\mathbf{V}$  is an  $N \times L$  matrix, the columns of which are vectors  $\mathbf{v}_i$ ;

$\mathbf{1}$  is the  $L \times L$  identity matrix.

We apply this formula to the deflated system matrix  $\mathbf{M}$ , defined as in (6), and to the deflated system matrix with unit conductivity differences  $\widetilde{\mathbf{M}}$  defined as

$$\widetilde{\mathbf{M}} = \widetilde{\mathbf{A}} + \frac{1}{N} \mathbf{e}\mathbf{e}^T \quad (17)$$

where  $\mathbf{e}$  is the vector defined in (6).

In order to apply (12), (9) is rewritten in terms of the deflated versions of  $\mathbf{A}$  and  $\widetilde{\mathbf{A}}$  as

$$\begin{aligned} \mathbf{M} &= \left( \widetilde{\mathbf{M}} - \frac{1}{N} \mathbf{e}\mathbf{e}^T \right) \Lambda_1 + \Lambda_2 + \frac{1}{N} \mathbf{e}\mathbf{e}^T \\ &= \widetilde{\mathbf{M}}\Lambda_1 + \frac{1}{N} \mathbf{e}\mathbf{e}^T (\mathbf{I} - \Lambda_1) + \Lambda_2 \end{aligned} \quad (18)$$

where  $\Lambda_1$  and  $\Lambda_2$  are defined as in (10) and (11), respectively.

Manipulating (18), one arrives at

$$\mathbf{M} = \widetilde{\mathbf{M}}\Lambda_1 + \mathbf{u}_d \mathbf{v}_d^T + \sum_{k=0}^{N_1+N_2-1} \mathbf{u}_k \mathbf{v}_k^T \quad (19)$$

where

$\mathbf{u}_k$  is an  $N \times 1$  column vector with its  $(N_0 + k)^{th}$  element equal to 1 and the other elements are 0;

$\mathbf{v}_k$  is an  $N \times 1$  column vector where the  $(N_0 + k)^{th}$  element is equal to  $\beta_k$  and the other elements are 0

$$\mathbf{v}_k = \begin{bmatrix} 0 \\ \vdots \\ 0 \\ \beta_k \\ 0 \\ \vdots \\ 0 \end{bmatrix} \} (N_0 + k)^{th} \text{ element} \quad (20)$$

where

$$\beta_k = \begin{cases} 2\sigma_0 - \sigma_1, & 0 \leq k < N_1 \\ 3\sigma_1 - 2\sigma_2, & N_1 \leq k < N_1 + N_2 \end{cases} \quad (21)$$

$$\mathbf{u}^d = \mathbf{e};$$

$\mathbf{v}_d$  is an  $N \times 1$  column vector defined as

$$\mathbf{v}_d = \frac{1}{N} \begin{bmatrix} 1 - (0 - \sigma_0) \\ \vdots \\ 1 - (0 - \sigma_0) \\ 1 - (\sigma_0 - \sigma_1) \\ \vdots \\ 1 - (\sigma_0 - \sigma_1) \\ 1 - (\sigma_1 - \sigma_2) \\ \vdots \\ 1 - (\sigma_1 - \sigma_2) \end{bmatrix} \left. \begin{array}{l} \left. \begin{array}{l} \vdots \\ \vdots \end{array} \right\} N_0 \times 1 \\ \left. \begin{array}{l} \vdots \\ \vdots \end{array} \right\} N_1 \times 1 \\ \left. \begin{array}{l} \vdots \\ \vdots \end{array} \right\} N_2 \times 1 \end{array} \right\} \quad (22)$$

Apart from  $\Lambda_1$ , this formulation is equivalent to the formulation of the Sherman–Morrison formula, as shown in (12).

At each of the iterations of the minimization procedure, the change of matrix  $\mathbf{M}$  is of rank  $N_1 + N_2 + 1$ . Furthermore, there is an additional complication caused by the diagonal matrix  $\Lambda_1$ , which also changes when the electrical conductivities are adjusted. However, its computation is quite straightforward and its effect is to add a multiplication factor to the columns of matrix  $\widetilde{\mathbf{M}}$ . The application of the Sherman–Morrison formula requires the definition of matrices  $\mathbf{Z}$ ,  $\mathbf{V}$ , and  $\mathbf{B}$ .

$\mathbf{Z}$  is the  $N \times N_{12}$  matrix in which the columns are the vectors  $\mathbf{z}_i$  and where  $N_{12} = N_1 + N_2 + 1$ . Vectors  $\mathbf{z}_i$  are the solutions to the equations

$$\widetilde{\mathbf{M}}\Lambda_1 \mathbf{z}_i = \mathbf{u}_i \quad (23)$$

where  $0 \leq i < N_{12}$  and  $\mathbf{u}_{N_1+N_2} = \mathbf{u}_d$ ;

$\mathbf{V}$  is the  $N \times N_{12}$  matrix in which the columns are the vectors  $\mathbf{v}_i$ , where  $0 \leq i < N_{12}$  and  $\mathbf{v}_{N_1+N_2} = \mathbf{v}_d$ . The explicit form of  $\mathbf{V}$  is given by

$$\mathbf{V} = \begin{bmatrix} \vdots & \vdots & \vdots & \frac{1-(0-\sigma_0)}{N} \\ \vdots & \vdots & \vdots & \vdots \\ \vdots & \vdots & \vdots & \frac{1-(0-\sigma_0)}{N} \\ \vdots & \vdots & \vdots & \frac{1-(\sigma_0-\sigma_1)}{N} \\ \vdots & \vdots & \vdots & \vdots \\ \vdots & \vdots & \vdots & \vdots \\ \vdots & \vdots & \vdots & \frac{1-(\sigma_0-\sigma_1)}{N} \\ \vdots & \vdots & \vdots & \frac{1-(\sigma_1-\sigma_2)}{N} \\ \vdots & \vdots & \vdots & \vdots \\ \vdots & \vdots & \vdots & \vdots \\ \vdots & \vdots & \vdots & \frac{1-(\sigma_1-\sigma_2)}{N} \end{bmatrix} \left. \begin{array}{l} \left. \begin{array}{l} \vdots \\ \vdots \end{array} \right\} N_0 \times N_{12} \\ \left. \begin{array}{l} \vdots \\ \vdots \end{array} \right\} N_1 \times N_{12} \\ \left. \begin{array}{l} \vdots \\ \vdots \end{array} \right\} N_2 \times N_{12} \end{array} \right\} \quad (24)$$

where  $C_0 = (2\sigma_0 - \sigma_1)$  and  $C_1 = (3\sigma_1 - 2\sigma_2)$ ;

$\mathbf{B}$  is the  $N_{12} \times N_{12}$  matrix defined as

$$\mathbf{B} = \mathbf{1} + \mathbf{V}^T \mathbf{Z}. \quad (25)$$

The explicit form of  $\mathbf{B}$  is given by (26) and (27) at bottom of the next page and  $\mathbf{z}_{i,k}$  is the  $k$ th component of the vector  $\mathbf{z}_i$  as defined previously.

The vectors  $\Psi'$  and  $\mathbf{x}'$  are found from the following equations:

$$\widetilde{\mathbf{M}}\Lambda_1 \Psi' = \Gamma \mathbf{J} \quad (28)$$

$$\mathbf{B}\mathbf{x}' = \mathbf{V}^T \Psi'. \quad (29)$$

Afterwards, the solution  $\Psi$  to (4) is found by the following expression:

$$\Psi = \Psi' - \mathbf{Z}\mathbf{x}' \quad (30)$$

where  $\Psi'$  is the solution to the undisturbed system.

The advantage of the application of the Sherman–Morrison formula is to reduce the size of the matrix to be inverted with the consequent saving of computation time. In fact, from the initial situation implying the bulk recomputation and inversion of matrix  $\mathbf{M}$ , which is  $N \times N$ , we are left with the computation and inversion of matrix  $\mathbf{B}$ , which is  $N_{12} \times N_{12}$ . The simulations regarding the minimization of the numerical error associated to the EIT BEM model showed that, for a given total number of discretization points, the optimal condition is attained when more than 50% of the points are allocated to the skin (see Section IV). Thus, in this situation an effective reduction in the computation time is obtained by the application of the Sherman–Morrison formula. In these circumstances, the computation time on a Pentium PC with a 200-MHz CPU and 128 MB of RAM was approximately equal to 3 h.

### B. The Head Model

The head was described using a set of three nested compartments, representing, respectively, the scalp, the skull, and the brain. The shape of the compartments was derived from the segmentation of brain, skull, and scalp obtained from the MRI scans of each patient. For five of the subjects, the segmentation was obtained using the automatic method described in [27]. For Subject 5, segmentation was obtained using Curry Version 3.0 (Neuroscan, El Paso, TX), since the results obtained with the aforementioned method were not entirely satisfactory in what regards the shape of the brain, skull, and scalp compartments as well as the skull thickness.

The point distribution among the three surfaces depends on the conditions yielding the lowest numerical error associated with the BEM model. This corresponds to allocate 60% of the points to the scalp, 30% of the points to the skull, and 10% of the points to the brain (see Section IV). A local refinement of the grid was applied around the injection electrodes, in the case

of the EIT method, since it increased BEMs numerical accuracy (see Section IV). The total number of points used in the discretization of the three surfaces was set approximately equal to 3000.

### III. DATA ACQUISITION

The same data as in [2] were used in the present study. The data acquisition from six normal subjects was performed using the Omega MEG/EEG system (CTF Systems Inc., Vancouver, BC, Canada), with 64 electrodes positioned according to the extended 10–20 system. Electrode positions were determined according to the method described in [28]. Current was injected on a pair of electrodes while measuring the potential distribution on the remaining sensors, this procedure being repeated for several injection pairs. As explained in [2] the injection and extracting electrodes were positioned with a maximum separation in between them, and the reference electrode located approximately halfway between injection and extracting electrodes. Furthermore, the injection–extraction electrode pairs were chosen to cover the entire perimeter of the head and their number varied between seven and ten.

The current generator was fed with a sinusoidal signal of 60 Hz and 10 V pp and produced an electric current with the same frequency and wave shape, having an intensity of 10  $\mu\text{A}$  root mean square. Data were acquired at a rate of 1250 Hz, using on-line high and low-pass filters at 0.16 and 300 Hz, respectively. Epochs of 105 s were recorded for each injection pair, each epoch consisting of 32 trials of 3.28 s, recorded in sequence. Data preprocessing was performed according to Appendix B. To reduce bias in the estimated conductivities, it was decided to calibrate the EEG amplifiers with respect to a reference channel, just before each experiment. For that purpose, the same signal was fed to all channels and the resulting potentials  $V_{ij}$  were used to compute relative calibration factors as follows:

$$C_i = \frac{\sum_{j=0}^{N_s} V_{0j} V_{ij}}{\sum_{j=0}^{N_s} (V_{0j})^2} \quad (31)$$

where

$$\mathbf{B} = \begin{bmatrix} (2\sigma_0 - \sigma_1)\mathbf{z}_{0,N_0} + 1 & \cdots & (2\sigma_0 - \sigma_1)\mathbf{z}_{N_1+N_2,N_0} \\ \vdots & \ddots & \vdots \\ (2\sigma_0 - \sigma_1)\mathbf{z}_{0,N_0+N_1-1} & \cdots & (2\sigma_0 - \sigma_1)\mathbf{z}_{N_1+N_2,N_0+N_1-1} \\ \cdots & \cdots & \cdots \\ (3\sigma_1 - 2\sigma_2)\mathbf{z}_{0,N_0+N_1} & \cdots & (3\sigma_1 - 2\sigma_2)\mathbf{z}_{N_1+N_2,N_0+N_1} \\ \vdots & & \vdots \\ (3\sigma_1 - 2\sigma_2)\mathbf{z}_{0,N-1} & \cdots & (3\sigma_1 - 2\sigma_2)\mathbf{z}_{N_1+N_2,N-1} \\ \cdots & \cdots & \cdots \\ \alpha_0 & \cdots & 1 + \alpha_{N_1+N_2} \end{bmatrix} \quad (26)$$

where

$$\alpha_i = \sum_{k=0}^{N_0-1} \left( \frac{1 - (0 - \sigma_0)}{N} \right) \mathbf{z}_{i,k} + \sum_{k=N_0}^{N_0+N_1-1} \left( \frac{1 - (\sigma_0 - \sigma_1)}{N} \right) \mathbf{z}_{i,k} + \sum_{k=N_0+N_1}^{N-1} \left( \frac{1 - (\sigma_1 - \sigma_2)}{N} \right) \mathbf{z}_{i,k} \quad (27)$$

- $i$  is the channel index;
- $j$  is the time sample index;
- $N_S$  is the total number of samples;
- $V_{ij}$  is the signal measured on channel  $i$ , time sample  $j$ ;
- $V_{0j}$  is the signal measured on the channel used as calibration reference, at time sample  $j$ .

#### IV. RESULTS

##### A. Numerical Accuracy of the BEM Model

In order to study the accuracy of the BEM model, several simulations were performed where the results obtained by the analytic spherical model were compared with the BEM results, obtained using triangulated spheres derived from the analytic spherical model. The goal was to find the best distribution of surface points for a certain constant value of the total number of points. An error quantity was defined as

$$\Delta = \frac{\sum_{ij} (\Psi_{ij}^{\text{ANA}} - \lambda \Psi_{ij}^{\text{BEM}})^2}{\sum_{ij} (\Psi_{ij}^{\text{ANA}})^2} \quad (32)$$

where

- $i$  runs over the number of current injection electrode pairs;
- $j$  runs over the number of measuring electrode pairs;
- $\Psi_{ij}^{\text{ANA}}$  is the potential computed according to the analytic model [3] generated by current injection pair  $i$  on measuring electrode pair  $j$ ;
- $\Psi_{ij}^{\text{BEM}}$  is the potential computed according to the BEM model, generated by current injection pair  $i$  on measuring electrode pair  $j$ ;
- $\lambda$  is a multiplication factor computed in order to minimize (32) and it is defined as

$$\lambda = \frac{\sum_{ij} \Psi_{ij}^{\text{ANA}} \Psi_{ij}^{\text{BEM}}}{\sum_{ij} (\Psi_{ij}^{\text{BEM}})^2} \quad (33)$$

The goal of the  $\lambda$  parameter is to eliminate the global scaling error. In the EIT IP, this type of error only influences the absolute values of the resistivities but not the resistivity ratio. In the EEG IP, it would only influence the source strength.

The fraction of points allocated to the brain (fb), skull (fsk), and scalp (fsc) was varied, while the total number of points was kept approximately equal to 1600. The results shown here were obtained using flat triangles and linear interpolation for the potential [5].

The behavior of the error is represented in Fig. 2(a). The optimal situation is characterized by fsc = 60%, fsk = 30%, and fb = 10%, where the optimal situation is considered to be the one that corresponds to the lowest error as well as to the flattest error function, the latter very important to avoid biased estimations of  $\rho_{\text{skull}}/\rho_{\text{brain}}$ ,  $\rho_{\text{brain}}$ , and  $\rho_{\text{skull}}$ . Several other situations are also plotted for comparison. In particular, it can be seen that the error behavior in the case of the optimal point distribution is better than in the case of the situations characterized by fsc = 40%, 30% and fsk = 30%, 40%. In fact, for small ratios the error is much better and for higher ratios it is only slightly worse, the overall behavior being less biased. This finding is

particularly important if it is considered that the latter point distributions, assuming that the total number of points is approximately equally distributed among the three compartments, are often used in BEM computations. The fact that the minimization of  $\Delta$  implies that most points are allocated to the scalp and skull agrees with the fact that more points have to be taken into account in the areas where the potential gradients are steeper (scalp in the case of the EIT) in order to obtain a good numerical accuracy. The effect of performing a local refinement of the grid of points was also investigated in a series of simulations where only the optimal point distribution, as obtained from the previous simulations, was considered. The local refinement of the grid was applied around the injection electrodes and several values for the refinement distance (triangles within refinement distance from the refinement centre were subdivided in four subtriangles) were tested. The total number of points was again kept approximately equal to 1600. The results for the best situation in terms of error behavior are shown in Fig. 2(b) (“*With refinement*” curve) and the results corresponding to the case where no refinement is applied (“*Without refinement*” curve) are also shown for comparison. According to the results, the application of local refinement both decreases the error amplitude and improves the shape of the error function by flattening it. Therefore, it should be used in the computation of  $\rho_{\text{skull}}/\rho_{\text{brain}}$ ,  $\rho_{\text{brain}}$ , and  $\rho_{\text{skull}}$  in order to avoid biased estimations of these parameters. The results regarding the variation of the refinement distance, keeping the total number of points constant, showed that if the refinement distance is too small (e.g., 0.5 cm) then the improvement in error behavior is small. This is due to the fact that in order to keep the total number of points constant, the meshes have to be coarsened in the regions away from the refinement area. If the latter is too small, then it is the effect of coarsening the meshes that determines the error behavior.

The results of the behavior of  $\Delta$ , with  $\lambda$  set to 1 (thus accounting for the total error), showed that the optimal situation is also obtained for fsc = 60%, fsk = 30%, and fb = 10%. Therefore, this distribution not only minimizes the error associated to the resistivity ratio but also the error associated to the absolute resistivity values.

The results obtained using curved triangles were similar to the ones shown here. Since the use of this type of surface interpolation implies the increase in the computation time, it was not considered worthwhile to use it in the resistivity estimations.

##### B. Resistivity Estimation

For each subject, the equivalent electrical resistivities were computed using the EIT method. Local refinement was applied around the injection electrodes and the refinement distance is varied in such a way that the total number of points used in the BEM model (approximately 3000 points) is comparable among subjects. The obtained results are presented in Table I and the behavior of the cost functions is represented in Fig. 3. In Table II, the average values and the relative standard deviations associated to  $\rho_{\text{skull}}/\rho_{\text{brain}}$ ,  $\rho_{\text{brain}}$ , and  $\rho_{\text{skull}}$  are presented. The relative standard deviation is defined as

$$\text{SD}(\%) = \frac{(\sqrt{\Delta})}{\bar{x}} \times 100 \quad (34)$$

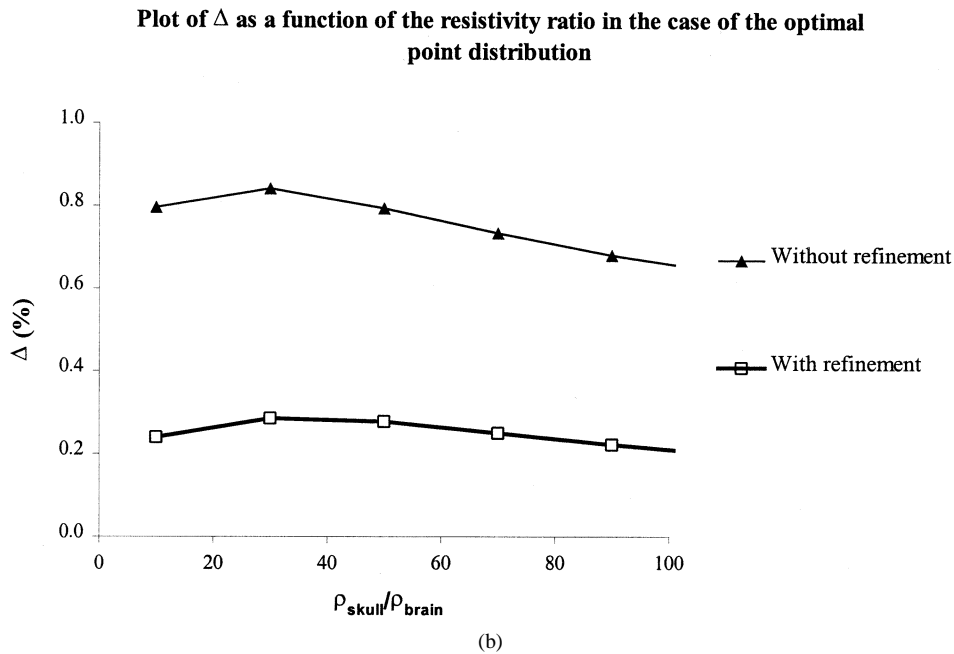
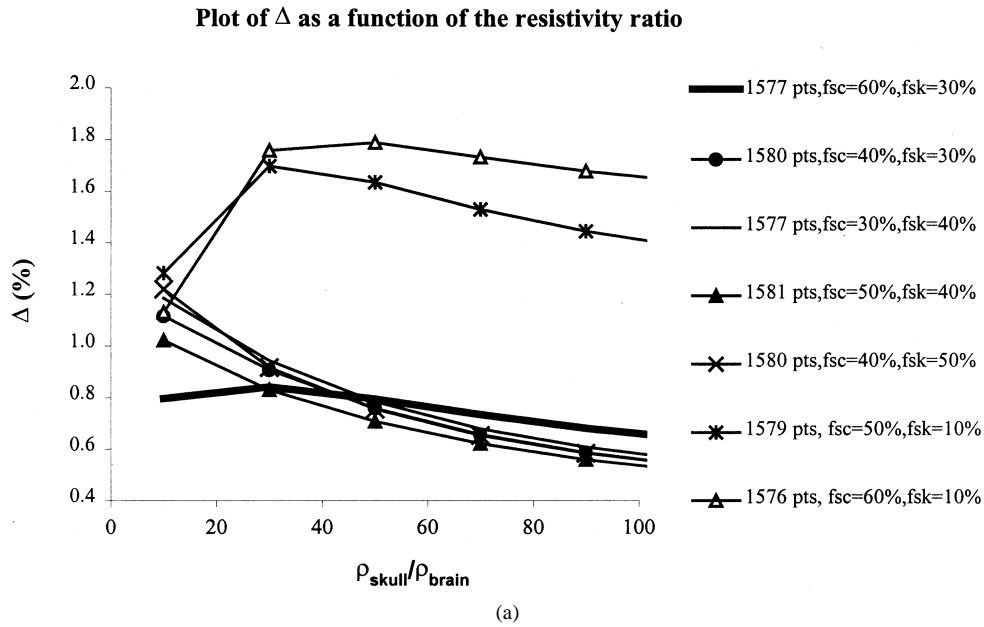


Fig. 2. (a) Plot of the numerical error  $\Delta$  as a function of  $\rho_{\text{skull}}/\rho_{\text{brain}}$ . Several situations, characterized by different fractions of scalp (fsc) and skull (fsk) points, are represented for comparison with the optimal situation (thick line). The latter is obtained for fsc = 60% and fsk = 30%. The first number in the legend is the total number of points used in the BEM model. (b) Plot of the numerical error  $\Delta$  as a function of  $\rho_{\text{skull}}/\rho_{\text{brain}}$  for the case where no local refinement is applied (*Without refinement*) and for the case where it is applied (*With refinement*). The total number of points used in the BEM model in the two situations is, respectively, equal to 1577 and 1554. The fraction of points in scalp, skull, and brain is, respectively, equal to 60%, 30%, and 10% and the refinement distance is equal to 2 cm.

where

$$\Delta = \left( \frac{\sum_{i=1}^6 (x_i - \bar{x})^2}{5} \right). \quad (35)$$

In (35),  $x$  can be identified with  $\rho_{\text{skull}}/\rho_{\text{brain}}$ ,  $\rho_{\text{brain}}$ , or  $\rho_{\text{skull}}$  and  $i$  runs over the number of subjects.

In Fig. 4, a scatterplot of  $\rho_{\text{skull}}$  against  $\rho_{\text{brain}}$  is presented containing data from the six subjects. The same scatterplot obtained using the spherical model [2] is represented in the same graph for comparison.

Fig. 3 shows that for five of the subjects, the minima of the cost functions are approximately located in the same range

of values of  $\rho_{\text{skull}}/\rho_{\text{brain}}$ . The cost function of Subject 6 is characterized by a steeper and slightly lower minimum. In Table I, it is seen that for Subjects 1 to 5 the values of  $\rho_{\text{skull}}/\rho_{\text{brain}}$ ,  $\rho_{\text{brain}}$ , and  $\rho_{\text{skull}}$  are very similar and, in particular, the variability in the resistivity of the skull is small. The results regarding Subject 6 differ slightly from those obtained for the other subjects such that the values concerning  $\rho_{\text{skull}}/\rho_{\text{brain}}$  and  $\rho_{\text{skull}}$  are slightly lower. The observation of Fig. 4 allows the comparison between the variability in the values of  $\rho_{\text{brain}}$  and  $\rho_{\text{skull}}$  for spherical [2] and realistic models. It can be seen that there is a clear trend of decrease in the variation (ratio between maximum

TABLE I

RESISTIVITY ESTIMATIONS OBTAINED WITH THE EIT METHOD USING REALISTIC MODELS. IN THE COLUMN SPECIFYING THE SUBJECTS, THE INFORMATION IN BETWEEN BRACKETS GIVES THE GENDER (M—MALE, F—FEMALE) AND AGE OF THE SUBJECTS

Subject	$\rho_{\text{brain}}$ ( $\Omega \cdot \text{cm}$ )	$\rho_{\text{skull}}$ ( $\Omega \cdot \text{cm}$ )	$\rho_{\text{skull}}/\rho_{\text{brain}}$
1 (f, 27 y)	333	11928	36
2 (m, 41 y)	292	12344	42
3 (f, 34 y)	292	14217	49
4 (m, 40 y)	311	13598	44
5 (m, 27 y)	234	13174	56
6 (f, 25 y)	346	8119	23

TABLE II

AVERAGE VALUES OF  $\rho_{\text{skull}}/\rho_{\text{brain}}$ ,  $\rho_{\text{brain}}$ , AND  $\rho_{\text{skull}}$  COMPUTED FROM THE RESULTS CORRESPONDENT TO THE SIX SUBJECTS. IN ADDITION, THE CORRESPONDENT RELATIVE STANDARD DEVIATION (SD) IS ALSO COMPUTED. IT IS DEFINED AS  $\text{SD}(\%) = (\sqrt{\Delta})/\bar{x} \times 100$  WHERE  $\Delta = ((\sum_{i=1}^6 (x_i - \bar{x})^2)/5)$

	Average	SD (%)
$\rho_{\text{skull}}/\rho_{\text{brain}}$	42	27
$\rho_{\text{brain}}$ ( $\Omega \cdot \text{cm}$ )	301	13
$\rho_{\text{skull}}$ ( $\Omega \cdot \text{cm}$ )	12230	18

also on the *in vivo* determination of the electrical resistivities of brain and skull [18]–[21]. In this paper, we show that with this EIT-based method it is possible to do the *in vivo* computation of the equivalent values of  $\rho_{\text{skull}}/\rho_{\text{brain}}$ ,  $\rho_{\text{skull}}$ , and  $\rho_{\text{brain}}$  individually for each subject using realistic models for the head. In this context, the equivalent values are those that minimize the systematic errors of the EEG IP [3] and may not be necessarily coincident with the true ones.

The dependence of the BEM model accuracy on the point distribution among surfaces and on the values of  $\rho_{\text{skull}}/\rho_{\text{brain}}$  generates highly biased estimations if the best conditions are not used in the computations. According to the results regarding the forward problem simulations, it was concluded that the situation yielding the best error behavior is obtained when most of the points are allocated to the scalp (60%) and skull (30%). This particular point distribution makes the use of the Sherman–Morrison formula particularly efficient since the matrices that have to be manipulated in the computations have their size decreased by 60%, which means a decrease in the computation time by more than a factor of 5. In addition, a local refinement of the point grid around the injection electrodes is also efficient in improving BEM accuracy.

The results obtained for  $\rho_{\text{skull}}/\rho_{\text{brain}}$  show that for the six subjects the correspondent values are within the same range. However, even though the values are quite similar, there is still some variation to be taken into account, especially when the results of Subjects 5 and 6 are considered. The effect of the bias on the estimations of the resistivities is studied by comparing the results obtained with approximately 3000 points with those obtained when reducing the total number of points to approximately 2000. For most of the subjects, the deviations in the values of  $\rho_{\text{skull}}/\rho_{\text{brain}}$ ,  $\rho_{\text{brain}}$ , and  $\rho_{\text{skull}}$  do not exceed 10%, being that the higher deviations are associated with  $\rho_{\text{skull}}/\rho_{\text{brain}}$  and  $\rho_{\text{skull}}$ . However, for Subject 3, the deviation in the results is larger (25% deviation in  $\rho_{\text{skull}}/\rho_{\text{brain}}$ ). In order to determine whether the results obtained with approximately 3000 points were still heavily influenced by the bias effect, further computations were performed for this subject using approximately 4000 points. The deviation in the results decreased to approximately 4%. The increase in the total number of points used in the BEM model beyond 3000 implies a considerable increase in the computation time and does not carry significant additional precision to the results. On the other hand, the observed bias can also be partially explained not only by the errors associated to

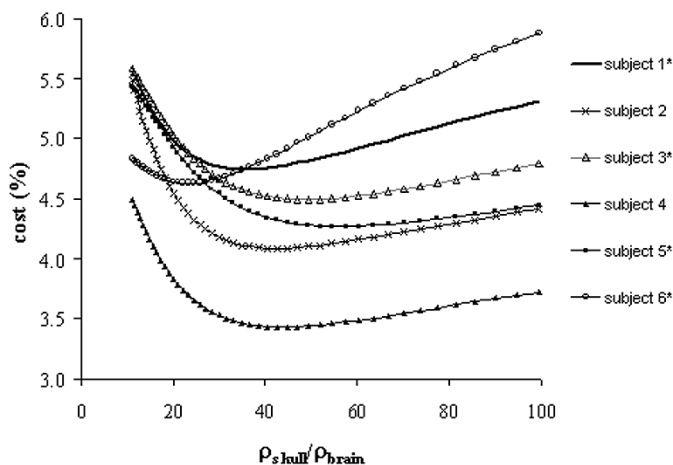


Fig. 3. Plot of the EIT cost functions for all subjects. The symbol \* means that the corresponding cost functions were shifted downwards in order to plot all cost functions in the same scale. The maximum applied shift was  $-7\%$  in the case of Subject 1.

and minimum values) of  $\rho_{\text{brain}}$  and  $\rho_{\text{skull}}$  when using realistic models. Taking as an example the values of  $\rho_{\text{skull}}$ , in the case of the spherical model the variation is even slightly higher than a factor of 2. In the case of the realistic models, this variation decreases to a factor of 1.75 if Subject 6 is included or to a factor of 1.19 if Subject 6 is not included.

## V. DISCUSSION AND CONCLUSION

The EEG IP is very dependent on the electrical properties of the volume conductor. In particular, when dealing with BEM models (where only the equivalent electric resistivities of each compartment need to be considered) the value of  $\rho_{\text{skull}}/\rho_{\text{brain}}$  is very important in determining the final solution [12]. Several recent studies [29], [30] have been focused on the effect of correctly modeling the skull resistivity on source location and

**Plot of the resistivity of the skull as a function of the resistivity of the brain**

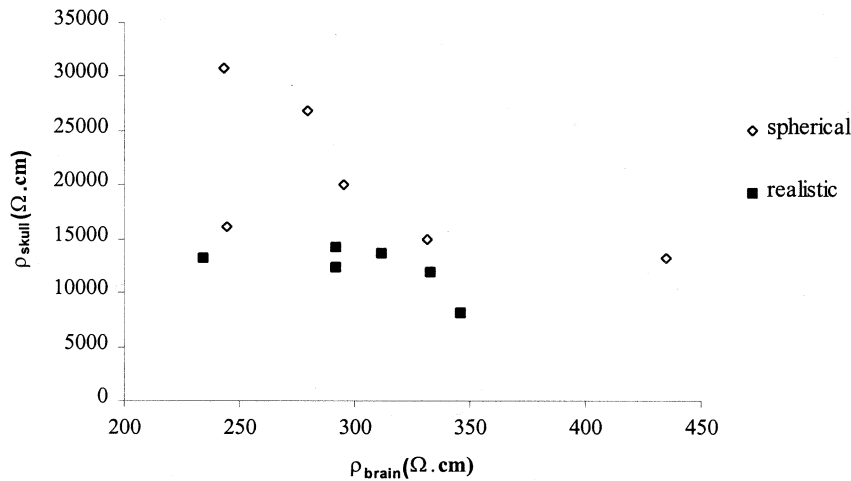


Fig. 4. Plot of the resistivity of the skull as a function of the resistivity of the brain, obtained with the EIT method using both spherical and realistic models. The results with the spherical model were obtained using the same relative skull thickness for all subjects, as presented in [2].

the BEM model but also due to slight geometry changes when the total number of points is changed. The change in the sizes of the meshes associated with the three compartments may generate slight variations in the skull thickness which in turn, due to the compensation ability of this EIT method [3], generate slight variations in the values of  $\rho_{\text{skull}}/\rho_{\text{brain}}$ ,  $\rho_{\text{brain}}$ , and  $\rho_{\text{skull}}$ . The latter values, as concluded in [3], are those that best compensate for geometrical variations in the head model. Therefore, taking into account the goal of this study, which is to determine *equivalent* values of  $\rho_{\text{skull}}/\rho_{\text{brain}}$ ,  $\rho_{\text{brain}}$ , and  $\rho_{\text{skull}}$ , it was considered that using 3000 points in the BEM model constituted a good choice in terms of tradeoff between computation time and precision required in the estimations.

When compared with the results presented by Oostendorp *et al.* [18], who was the first to apply EIT to the estimation of equivalent electrical resistivities using BEM, the values of  $\rho_{\text{skull}}/\rho_{\text{brain}}$  presented in this paper are higher and only the value correspondent to Subject 6 falls within the same range. Several factors can explain the difference in the results. Only two subjects were studied in [18] and it may be that they are characterized by a lower skull-to-brain resistivity ratio, as it is the case of Subject 6 presented in this paper. In addition, the results in [18] were computed from data of only two injection pairs whereas in the present study several injection electrodes were chosen in order to cover the whole perimeter of the head. This generates a different sensitivity of the method toward local variations in the skull thickness and geometry [31]. Finally, the BEM models used in [18] may be characterized by skull thicknesses that are too large, which would explain the lower obtained values for  $\rho_{\text{skull}}/\rho_{\text{brain}}$ .

The comparison with the results obtained in [2] using spherical models to describe the head indicates a clear trend of decrease in the variation of  $\rho_{\text{skull}}/\rho_{\text{brain}}$ ,  $\rho_{\text{skull}}$ , and  $\rho_{\text{brain}}$  among subjects. In fact, the use of realistic models reduced the variation associated to these parameters by half. If considerable systematic errors are associated to the head model, like in the

case of spherical models, then the estimated resistivity values and the resistivity ratio will tend to compensate for them and, therefore, may be quite far from the realistic values, thus increasing the differences among subjects. Then it should be concluded that the correction of the head geometry, both in terms of shape and skull thickness, is very important to compute realistic values of  $\rho_{\text{skull}}/\rho_{\text{brain}}$ ,  $\rho_{\text{skull}}$ , and  $\rho_{\text{brain}}$ . However, even though the use of realistic models significantly decreased the variability in resistivity values and in the resistivity ratio, some variation remains to be accounted for (see Table II), in particular when the results regarding Subjects 5 and 6 are considered (see Table I). For these subjects, a factor of 2.4 exists between the corresponding values of  $\rho_{\text{skull}}/\rho_{\text{brain}}$  being that the largest difference is associated to the resistivity of the skull. Considering the complex structure of the skull [31], [32], the existence of variations in the skull resistivity among subjects due to natural causes is not unexpected. Such differences should not be disregarded, especially when dealing with the EEG IP [30]. We hope to increase the number of subjects in the future in order to confirm this trend. For that, we will need a specific measurement system which is not yet available.

In [2], a comparison between EIT and the combined analysis of MEG/EEG data [20], [33], [34] was made for spherical models. In the course of the study that led to the present paper, an attempt was made to do the same comparison using realistic models. However, numerical complications made this comparison impossible and, therefore, the results of such a comparison are not presented in this paper. However, it is important to discuss the sources of the numerical problems. As for the case of EIT, a thorough study of the BEM accuracy was performed through a series of simulations with the EEG forward problem. It was found that even in the best conditions (70% of the points allocated to the brain) the dependence of the systematic errors associated to BEM is much stronger than in the case of EIT, showing a clear bias toward lower values of  $\rho_{\text{skull}}/\rho_{\text{brain}}$ . In addition, the amplitude of the error

is larger. As a consequence, the minimum of the cost function obtained using a triangulated spherical model shows a clear shift toward lower ratios when compared with the minimum given by the analytic spherical model. Even with the use of as many as 4200 points in the BEM model, a difference of 14% was found between the numerical and analytic minimum and, therefore, a minimum of 5000 points should be considered in the computations. The optimal point distribution in the EEG case, where only 10% of the points are allocated to the scalp, makes the application of the Sherman–Morrison formula much less efficient and increases enormously the computation time. Therefore, our attempts to estimate the values of  $\rho_{\text{skull}}/\rho_{\text{brain}}$ ,  $\rho_{\text{skull}}$ , and  $\rho_{\text{brain}}$  using the combined analysis of somatosensory evoked fields and somatosensory evoked potentials (SEF/SEP) are postponed until a faster computer or improved BEM algorithms are available.

The results presented in this paper clearly show the feasibility of the proposed EIT method to perform *in vivo* estimations of  $\rho_{\text{skull}}/\rho_{\text{brain}}$ ,  $\rho_{\text{skull}}$ , and  $\rho_{\text{brain}}$  using realistic models for the head. The results also show that the ratio between the resistivities of skull and brain is more likely to be in the range of 20–50 rather than equal to the commonly accepted value of 80. Another important point is related to the fact that, even with head geometry correction, there are still variations to be accounted for, thus pointing to the necessity of calibrating the values of  $\rho_{\text{skull}}/\rho_{\text{brain}}$ ,  $\rho_{\text{skull}}$ , and  $\rho_{\text{brain}}$  by measuring them *in vivo* for each subject. We think that the proposed EIT method is not only able to fulfil this goal but also has technical requirements usually available in any EEG laboratory.

#### APPENDIX A SIMPLIFICATION OF THE SYSTEM MATRIX $\mathbf{A}$

The explicit form of matrix  $\mathbf{A}$  is given below in terms of the submatrices  $\mathbf{A}^{ij}$

$$\mathbf{A} = \frac{1}{4\pi} \begin{bmatrix} \mathbf{A}^{00} & \mathbf{A}^{01} & \mathbf{A}^{02} \\ \mathbf{A}^{10} & \mathbf{A}^{11} & \mathbf{A}^{12} \\ \mathbf{A}^{20} & \mathbf{A}^{21} & \mathbf{A}^{22} \end{bmatrix} \quad (\text{A.1})$$

In (A.1) the submatrices are given as

$$\mathbf{A}^{00} = \begin{bmatrix} a_{11}^{00} & a_{12}^{00} & \cdots & \cdots & a_{1N_0}^{00} \\ a_{21}^{00} & \ddots & & & \vdots \\ \vdots & & \ddots & & \vdots \\ \vdots & & & \ddots & \vdots \\ a_{N_0 1}^{00} & a_{N_0 2}^{00} & \cdots & a_{N_0(N_0-1)}^{00} & a_{N_0 N_0}^{00} \end{bmatrix} \quad (\text{A.2})$$

where

$$a_{11}^{00} = 4\pi\sigma_0 - \sigma_0\Omega_{00}^{00}; \quad (\text{A.2.a})$$

$$a_{12}^{00} = -\sigma_0\Omega_{01}^{00}; \quad (\text{A.2.b})$$

$$a_{1N_0}^{00} = -\sigma_0\Omega_{0(N_0-1)}^{00}; \quad (\text{A.2.c})$$

$$a_{21}^{00} = -\sigma_0\Omega_{10}^{00}; \quad (\text{A.2.d})$$

$$a_{(N_0-1)N_0}^{00} = -\sigma_0\Omega_{(N_0-2)(N_0-1)}^{00}; \quad (\text{A.2.e})$$

$$a_{N_0 1}^{00} = -\sigma_0\Omega_{(N_0-1)0}^{00}; \quad (\text{A.2.f})$$

$$a_{N_0 2}^{00} = -\sigma_0\Omega_{(N_0-1)1}^{00}; \quad (\text{A.2.g})$$

$$a_{N_0(N_0-1)}^{00} = -\sigma_0\Omega_{(N_0-1)(N_0-2)}^{00}; \quad (\text{A.2.h})$$

$$a_{N_0 N_0}^{00} = 4\pi\sigma_0 - \sigma_0\Omega_{(N_0-1)(N_0-1)}^{00}. \quad (\text{A.2.i})$$

$$\mathbf{A}^{01} = \begin{bmatrix} -(\sigma_1 - \sigma_0)\Omega_{0N_0}^{01} & \cdots & -(\sigma_1 - \sigma_0)\Omega_{0(N_0+N_1-1)}^{01} \\ \vdots & \ddots & \vdots \\ -(\sigma_1 - \sigma_0)\Omega_{(N_0-1)N_0}^{01} & \cdots & -(\sigma_1 - \sigma_0)\Omega_{(N_0-1)(N_0+N_1-1)}^{01} \end{bmatrix} \quad (\text{A.3})$$

$$\mathbf{A}^{02} = \begin{bmatrix} -(\sigma_2 - \sigma_1)\Omega_{0N_0 1}^{02} & \cdots & -(\sigma_2 - \sigma_1)\Omega_{0(N_1-1)}^{02} \\ \vdots & \ddots & \vdots \\ -(\sigma_2 - \sigma_1)\Omega_{(N_0-1)N_0 1}^{02} & \cdots & -(\sigma_2 - \sigma_1)\Omega_{(N_0-1)(N_1-1)}^{02} \end{bmatrix} \quad (\text{A.4})$$

$$\mathbf{A}^{10} = \begin{bmatrix} -\sigma_0\Omega_{N_0 0}^{10} & \cdots & -\sigma_0\Omega_{N_0(N_0-1)}^{10} \\ \vdots & \ddots & \vdots \\ -\sigma_0\Omega_{(N_0 1)0}^{10} & \cdots & -\sigma_0\Omega_{(N_0 1)(N_0-1)}^{10} \end{bmatrix} \quad (\text{A.5})$$

$$\mathbf{A}^{11} = \begin{bmatrix} a_{11}^{11} & a_{12}^{11} & \cdots & \cdots & a_{1N_1}^{11} \\ a_{21}^{11} & \ddots & & & \vdots \\ \vdots & & \ddots & & \vdots \\ \vdots & & & \ddots & \vdots \\ a_{N_1 1}^{11} & a_{N_1 2}^{11} & \cdots & a_{N_1(N_1-1)}^{11} & a_{N_1 N_1}^{11} \end{bmatrix} \quad (\text{A.6})$$

In the abovementioned equations and also (A.6.a)–(A.10.h) (shown at the top of the next page), the symbols are defined as

- $\sigma_0$ ,  $\sigma_1$ , and  $\sigma_2$  are the inner conductivities of scalp, skull, and brain, respectively;
- $\Omega_{ij}^{km}$  is the solid angle as defined in (2);
- $N_0$ ,  $N_1$ , and  $N_2$  are, respectively, the number of nodes of surfaces  $S_0$ ,  $S_1$ , and  $S_2$ , corresponding to scalp, skull, and brain;
- $N_{01} = N_0 + N_1$  is the number of nodes of scalp and skull;
- $N = N_0 + N_1 + N_2$  is the total number of nodes.

$$\left\{ \begin{array}{l} A_{jj}^{00} = \sigma_0 \sum_{j'=0, j' \neq j}^{N_0-1} \Omega_{jj'}^{00} + (\sigma_1 - \sigma_0) \sum_{j'=N_0}^{N_0+N_1-1} \Omega_{jj'}^{01} \\ \quad + (\sigma_2 - \sigma_1) \sum_{j'=N_0+N_1}^{N-1} \Omega_{jj'}^{02}, \quad 0 \leq j < N_0 \\ A_{jj}^{11} = \sigma_0 \sum_{j'=0}^{N_0-1} \Omega_{jj'}^{10} + (\sigma_1 - \sigma_0) \sum_{j'=N_0, j' \neq j}^{N_0+N_1-1} \Omega_{jj'}^{11} \\ \quad + (\sigma_2 - \sigma_1) \sum_{j'=N_0+N_1}^{N-1} \Omega_{jj'}^{12}, \quad N_0 \leq j < N_0 + N_1 \\ A_{jj}^{22} = \sigma_0 \sum_{j'=0}^{N_0-1} \Omega_{jj'}^{20} + (\sigma_1 - \sigma_0) \sum_{j'=N_0}^{N_0+N_1-1} \Omega_{jj'}^{21} \\ \quad + (\sigma_2 - \sigma_1) \sum_{j'=N_0+N_1, j' \neq j}^{N-1} \Omega_{jj'}^{22}, \quad N_0 + N_1 \leq j < N. \end{array} \right. \quad (\text{A.11})$$

Since the solid angles  $\Omega_{ii}^{kk}$  are ill-defined, the computation of the diagonals of matrix  $\mathbf{A}$  is done according to the procedure described in [5]. Furthermore, the method used to determine the diagonals of matrix  $\mathbf{A}$  influences the form of matrices  $\Lambda_1$  and

$$a_{11}^{11} = 4\pi\sigma_1 - (\sigma_1 - \sigma_0)\Omega_{N_0 N_0}^{11}; \quad (\text{A.6.a})$$

$$a_{12}^{11} = -(\sigma_1 - \sigma_0)\Omega_{N_0(N_0+1)}^{11}; \quad (\text{A.6.b})$$

$$a_{1N_1}^{11} = -(\sigma_1 - \sigma_0)\Omega_{N_0(N_0+1)}^{11}; \quad (\text{A.6.c})$$

$$a_{21}^{11} = -(\sigma_1 - \sigma_0)\Omega_{(N_0+1)N_0}^{11}; \quad (\text{A.6.d})$$

$$a_{(N_1-1)(N_1-1)}^{11} = -(\sigma_1 - \sigma_0)\Omega_{(N_0+2)(N_0+1)}^{11}; \quad (\text{A.6.e})$$

$$a_{N_{11}}^{11} = -(\sigma_1 - \sigma_0)\Omega_{(N_0+1)N_0}^{11}; \quad (\text{A.6.f})$$

$$a_{N_{12}}^{11} = -(\sigma_1 - \sigma_0)\Omega_{(N_0+1)(N_0+1)}^{11}; \quad (\text{A.6.g})$$

$$a_{N_1(N_1-1)}^{11} = -(\sigma_1 - \sigma_0)\Omega_{(N_0+1)(N_0+2)}^{11}; \quad (\text{A.6.h})$$

$$a_{N_1 N_1}^{11} = 4\pi\sigma_1 - (\sigma_1 - \sigma_0)\Omega_{(N_0+1)(N_0+1)}^{11}. \quad (\text{A.6.i})$$

$$\mathbf{A}^{12} = \begin{bmatrix} -(\sigma_2 - \sigma_1)\Omega_{N_0 N_0}^{12} & \cdots & -(\sigma_2 - \sigma_1)\Omega_{N_0(N-1)}^{12} \\ \vdots & \ddots & \vdots \\ -(\sigma_2 - \sigma_1)\Omega_{(N_0+1)N_0}^{12} & \cdots & -(\sigma_2 - \sigma_1)\Omega_{(N_0+1)(N-1)}^{12} \end{bmatrix} \quad (\text{A.7})$$

$$\mathbf{A}^{20} = \begin{bmatrix} -\sigma_0\Omega_{N_0 0}^{20} & \cdots & -\sigma_0\Omega_{N_0(N_0-1)}^{20} \\ \vdots & \ddots & \vdots \\ -\sigma_0\Omega_{(N-1)0}^{20} & \cdots & -\sigma_0\Omega_{(N-1)(N_0-1)}^{20} \end{bmatrix} \quad (\text{A.8})$$

$$\mathbf{A}^{21} = \begin{bmatrix} -(\sigma_1 - \sigma_0)\Omega_{N_0 N_0}^{21} & \cdots & -(\sigma_1 - \sigma_0)\Omega_{N_0(N_0+1)}^{21} \\ \vdots & \ddots & \vdots \\ -(\sigma_1 - \sigma_0)\Omega_{(N-1)N_0}^{21} & \cdots & -(\sigma_1 - \sigma_0)\Omega_{(N-1)(N_0+1)}^{21} \end{bmatrix} \quad (\text{A.9})$$

$$\mathbf{A}^{22} = \begin{bmatrix} a_{11}^{22} & a_{12}^{22} & \cdots & \cdots & a_{1N_2}^{22} \\ a_{21}^{22} & \ddots & & & \\ \vdots & \ddots & & & \\ \vdots & & \ddots & & a_{(N_2-1)N_2}^{22} \\ a_{N_2 1}^{22} & \cdots & \cdots & a_{N_2(N_2-1)}^{22} & a_{N_2 N_2}^{22} \end{bmatrix} \quad (\text{A.10})$$

$$a_{11}^{22} = 4\pi\sigma_2 - (\sigma_2 - \sigma_1)\Omega_{N_0 N_0}^{22}; \quad (\text{A.10.a})$$

$$a_{12}^{22} = -(\sigma_2 - \sigma_1)\Omega_{N_0(N_0+1)}^{22}; \quad (\text{A.10.b})$$

$$a_{1N_2}^{22} = -(\sigma_2 - \sigma_1)\Omega_{N_0(N-1)}^{22}; \quad (\text{A.10.c})$$

$$a_{21}^{22} = -(\sigma_2 - \sigma_1)\Omega_{(N_0+1)N_0}^{22}; \quad (\text{A.10.d})$$

$$a_{(N_2-1)N_2}^{22} = -(\sigma_2 - \sigma_1)\Omega_{(N-2)(N-1)}^{22}; \quad (\text{A.10.e})$$

$$a_{N_{21}}^{22} = -(\sigma_2 - \sigma_1)\Omega_{(N-1)N_0}^{22}; \quad (\text{A.10.f})$$

$$a_{N_2(N_2-1)}^{22} = -(\sigma_2 - \sigma_1)\Omega_{(N-1)(N-2)}^{22}; \quad (\text{A.10.g})$$

$$a_{N_2 N_2}^{22} = 4\pi\sigma_2 - (\sigma_2 - \sigma_1)\Omega_{(N-1)(N-1)}^{22}. \quad (\text{A.10.h})$$

$\Lambda_2$  in (9). Thus, its definition is given explicitly in the following paragraphs: Since the solid angle subtended by a point outside or inside a surface equals, respectively, 0 or  $4\pi$  the expressions in (A.11) can be simplified to

$$\begin{cases} A_{jj}^{00} = \sigma_0 \sum_{j'=0, j' \neq j}^{N_0-1} \Omega_{jj'}^{00}, & 0 \leq j < N_0 \\ A_{jj}^{11} = \sigma_0 + (\sigma_1 - \sigma_0) \sum_{j'=N_0, j' \neq j}^{N_0+N_1-1} \Omega_{jj'}^{11}, & N_0 \leq j < N_0+N_1 \\ A_{jj}^{22} = \sigma_1 + (\sigma_2 - \sigma_1) \sum_{j'=N_0+N_1, j' \neq j}^{N-1} \Omega_{jj'}^{22}, & N_0+N_1 \leq j < N. \end{cases} \quad (\text{A.12})$$

The sums in (A.12) can be written in terms of the diagonals of matrix  $\tilde{A}$ , which is defined as matrix  $\tilde{A}$  with  $\sigma_0$  and the conductivity differences set to unity. The expressions in (A.12) are then written as

$$\begin{cases} A_{jj}^{00} = \sigma_0 \tilde{A}_{jj}^{00}, & 0 \leq j < N_0 \\ A_{jj}^{11} = \sigma_0 + (\sigma_1 - \sigma_0)(\tilde{A}_{jj}^{11} - 1) = (2\sigma_0 - \sigma_1) \\ \quad + (\sigma_1 - \sigma_0)\tilde{A}_{jj}^{11}, & N_0 \leq j < N_0+N_1 \\ A_{jj}^{22} = \sigma_1 + (\sigma_2 - \sigma_1)(\tilde{A}_{jj}^{22} - 2) = (3\sigma_1 - 2\sigma_2) \\ \quad + (\sigma_2 - \sigma_1)\tilde{A}_{jj}^{22}, & N_0+N_1 \leq j < N \end{cases} \quad (\text{A.13})$$

APPENDIX B  
 DATA PREPROCESSING

The wave shape of the injected current is known since it is coincident with the wave shape of the signal feeding the current generator. Since there is a linear relationship between injected current and measured potential, it is possible to correlate the latter with the signal feeding the current generator through a multiplication factor. This multiplication factor is taken as the constant potential value to be used in the EIT analysis. This idea is developed, in mathematical terms, along the next lines.

The potential measured on channel  $i$  at time sample  $j$  is written according to the model

$$v_{ij} = v_i v_j^{adc} + \varepsilon_{ij} \quad (\text{B.1})$$

where

$v_{ij}$  is the potential measured on channel  $i$  at time sample  $j$ ;

$v_j^{adc}$  is the potential feeding the current generator on time sample  $j$  normalized such that  $(1/N_{\text{samples}}) \sum_j (v_j^{adc})^2 = 1$ ;

$N_{\text{samples}}$  is the number of time samples;

$\varepsilon_{ij}$  is the noise contribution to the signal measured on channel  $i$ ;

$v_i$  is the amplitude of the potential value at electrode  $i$  to be used in EIT analysis.

The computation of  $v_i$  is performed in a least squares sense by solving the following equation:

$$\frac{\partial \left( \sum_j (v_{ij} - v_i v_j^{adc})^2 \right)}{\partial v_i} = 0 \quad (\text{B.2})$$

from which follows:

$$v_i = \frac{\sum_j v_j^{adc} v_{ij}}{\sqrt{N_{\text{samples}} \sum_j (v_j^{adc})^2}} \quad (\text{B.3})$$

where  $v_{ij}$  is the potential value measured on channel  $i$ , time sample  $j$ .

The estimations of noise power are computed considering the variations of the potential values computed for each trial ( $v_j^k$ ) around the mean ( $\bar{v}_i$ ). In this way, the estimations of noise power  $N$  are obtained according to

$$N = \sum_i (\text{StDev}_i)^2 \quad (\text{B.4})$$

where

$\text{StDev}_i = \frac{\sqrt{\sum_k (v_i^k - \bar{v}_i)^2 / N_{\text{trials}}}}$   $N_{\text{trials}}$ ;  $k$  runs over the number of trials,

$v_i^k$  is the potential value for channel  $i$ , trial  $k$ ;

$\bar{v}_i$  is the average of all  $v_i^k$  values, computed over  $N_{\text{trials}}$ .

The SNR is then defined accordingly as

$$\text{SNR} = \sqrt{\frac{\sum_i \bar{v}_i^2}{\sum_i (\text{StDev}_i)^2}} \quad (\text{B.5})$$

where  $i$  runs over the total number of channels.

Since the equivalent resistivities are assumed to be stationary in time, the measure of the signal reproducibility of each channel is taken as criterion to classify good and bad channels and as a method to quantify the reliability of the individual measurements. To measure reproducibility, the normalized standard deviation of each channel  $i$ ,  $\text{SDNorm}_i$ , is used

$$\text{SDNorm}_i(\%) = \frac{\text{StDev}_i}{\sqrt{\sum_i \bar{v}_i^2}} \times 100. \quad (\text{B.6})$$

The criterion to reject a channel from the computations was set at  $\text{SDNorm} > 0.5\%$ . All the recorded EIT data was characterized by values of SNR higher than 100.

## ACKNOWLEDGMENT

The authors would like to thank H. Goovaerts for his work in the design and manufacture of the current generator used in the data acquisition phase.

## REFERENCES

- [1] D. C. Barber and B. H. Brown, "Applied potential tomography," *J. Phys. E, Sci. Instrum.*, vol. 37, pp. 723–732, 1984.
- [2] S. Gonçalves, J. C. de Munck, J. P. A. Verbunt, R. M. Heethaar, and F. H. Lopes da Silva, "In vivo measurement of the brain and skull resistivities using an EIT-based method and the combined analysis of SEF/SEP data," *IEEE Trans. Biomed. Eng.*, 2003, to be published.
- [3] S. Gonçalves, J. C. de Munck, R. M. Heethaar, F. H. Lopes da Silva, and B. W. van Dijk, "The application of electrical impedance tomography to reduce systematic errors in the EEG inverse problem—a simulation study," *Physiol. Meas.*, vol. 21, pp. 379–393, 2000.
- [4] Z. J. Koles, "Trends in EEG source localization," *Electroencephalogr. Clin. Neurophysiol.*, vol. 106, pp. 127–137, 1998.
- [5] J. C. de Munck, "A linear discretization of the volume conductor boundary integral equation using analytically integrated elements," *IEEE Trans. Biomed. Eng.*, vol. 39, pp. 986–990, Sept. 1992.
- [6] J. C. de Munck and M. J. Peters, "A fast method to compute the potential in the multisphere model," *IEEE Trans. Biomed. Eng.*, vol. 40, pp. 1166–1174, Nov. 1993.
- [7] J. C. Moshier, R. M. Leahy, and P. S. Lewis, "EEG and MEG: forward solutions for inverse models," *IEEE Trans. Biomed. Eng.*, vol. 46, pp. 245–259, Mar. 1999.
- [8] J. Sarvas, "Basic mathematical and electromagnetic concepts of the bi-magnetic inverse problem," *Phys. Med. Biol.*, vol. 32, pp. 11–22, 1987.
- [9] J. C. Moshier, M. E. Spencer, R. M. Leahy, and P. S. Lewis, "Error bounds for EEG and MEG dipole source localization," *Electroencephalogr. Clin. Neurophysiol.*, vol. 86, pp. 303–321, 1993.
- [10] J. P. Ary, S. A. Klein, and D. H. Fender, "Location of sources of evoked scalp potentials: Corrections for skull and scalp thicknesses," *IEEE Trans. Biomed. Eng.*, vol. BME-28, pp. 447–452, June 1981.
- [11] Y. Eshel, S. Witman, M. Rosenfeld, and S. Abboud, "Correlation between skull thickness asymmetry and scalp potential estimated by a numerical model of the head," *IEEE Trans. Biomed. Eng.*, vol. 42, pp. 242–249, Mar. 1995.
- [12] G. Huiskamp, M. Vroeijsenstijn, R. van Dijk, G. Wieneke, and A. Huffelen, "The need to correct realistic geometry in the inverse EEG problem," *IEEE Trans. Biomed. Eng.*, vol. 46, pp. 1281–1287, Nov. 1999.
- [13] R. M. Leahy, J. C. Moshier, M. E. Spencer, M. X. Huang, and J. D. Lewine, "A study of dipole localization accuracy for MEG and EEG using a human skull phantom," *Electroencephalogr. Clin. Neurophysiol.*, vol. 107, pp. 159–173, 1998.
- [14] R. Pohlmeier, H. Buchner, A. Knoll, R. Beckmann, and J. Pesh, "The influence of skull—conductivity misspecification on inverse source localization in realistically shaped finite element models," *Brain Topogr.*, vol. 9, no. 3, pp. 157–162, 1997.
- [15] C. J. Stok, "The influence of model parameters on EEG/MEG single dipole source estimation," *IEEE Trans. Biomed. Eng.*, vol. BME-34, pp. 289–296, Apr. 1987.
- [16] L. A. Geddes and L. E. Baker, "The specific resistance of biological material—a compendium of data for the biomedical engineer and physiologist," *Med. Biol. Eng.*, vol. 5, pp. 271–293, 1967.

- [17] T. J. C. Faes, H. Van der Meij, J. C. de Munck, and R. M. Heethaar, "The resistivity of human tissue (100 Hz–10 MHz): a meta-analysis of review studies," *Physiol. Meas.*, vol. 20, no. 4, pp. R1–R10, 1999.
- [18] T. F. Oostendorp, J. Delbeke, and D. Stegeman, "The conductivity of the human skull: results of *in vivo* and *in vitro* measurements," *IEEE Trans. Biomed. Eng.*, vol. 47, pp. 1487–1493, Nov. 2000.
- [19] C. M. Towers, H. McCann, M. Wang, P. C. Beatty, C. J. D. Pomfrett, and M. S. Beck, "3D simulation of EIT for monitoring impedance variations within the human head," *Physiol. Meas.*, vol. 21, pp. 119–124, 2000.
- [20] H. M. Huizenga, T. L. van Zuijlen, D. J. Heslenfeld, and P. C. M. Moleenaar, "Simultaneous MEG and EEG source analysis," *Phys. Med. Biol.*, vol. 46, no. 7, pp. 1737–1751, 2001.
- [21] T. C. Ferree, K. J. Eriksen, and D. M. Tucker, "Regional head tissue conductivity estimation for improved EEG analysis," *IEEE Trans. Biomed. Eng.*, vol. 47, pp. 1584–1592, Dec. 2000.
- [22] M. Fuchs, M. Wagner, and J. Kastner, "Boundary element method volume conductor models for EEG source reconstruction," *Clin. Neurophys.*, vol. 112, pp. 1400–1407, 2001.
- [23] W. H. Press, B. P. Flannery, S. A. Teukolsky, and W. T. Wetterling, *Numerical Recipes in C*. Cambridge, U.K.: Cambridge Univ. Press, 1988.
- [24] T. Oostendorp and A. van Oosterom, "Source parameter estimation in inhomogeneous volume conductors of arbitrary shape," *IEEE Trans. Biomed. Eng.*, vol. 36, pp. 382–391, Mar. 1989.
- [25] M. Hämäläinen and J. Sarvas, "Realistic conductivity geometry model of the human head for interpretation of neuromagnetic data," *IEEE Trans. Biomed. Eng.*, vol. 36, pp. 165–171, Feb. 1989.
- [26] T. Oostendorp and A. van Oosterom, "The potential distribution generated by surface electrodes in inhomogeneous volume conductors of arbitrary shape," *IEEE Trans. Biomed. Eng.*, vol. 38, pp. 409–417, May 1991.
- [27] D. Van't Ent, J. C. de Munck, and A. L. Kaas, "An automated procedure for deriving realistic volume conductor models for MEG/EEG source localization," *IEEE Trans. Biomed. Eng.*, vol. 48, pp. 1434–1443, Dec. 2001.
- [28] J. C. de Munck, J. P. A. Verbunt, D. Van't Ent, and B. W. Van Dijk, "The use of an MEG device as 3D digitizer and motion monitoring system," *Phys. Med. Biol.*, vol. 46, pp. 2041–2052, 2001.
- [29] J. Ollikainen, M. Vauhkonen, P. Karjalainen, and J. Kaipio, "Effects of skull inhomogeneities on EEG source estimation," *Med. Eng. Phys.*, vol. 21, pp. 143–154, 1999.
- [30] B. Vanrumste, G. Van Hoey, R. Van de Walle, M. D'Havé, I. Lemahieu, and P. Boon, "Dipole location errors in electroencephalogram source analysis due to volume conductor model errors," *Med. Biol. Eng. Comput.*, vol. 38, pp. 528–534, 2000.
- [31] S. K. Law, "Thickness and resistivity variations over the upper surface of the human skull," *Brain Topogr.*, vol. 6, pp. 99–109, 1993.
- [32] M. Akhtari, H. C. Bryant, A. N. Mamelak, L. Heller, J. J. Shih, M. Mandelkern, A. Matlachov, D. M. Ranken, E. D. Best, and W. W. Sutherling, "Conductivities of three-layer human skull," *Brain Topogr.*, vol. 13, no. 1, pp. 29–42, 2000.
- [33] M. Fuchs, H. A. Wischmann, T. Köhler, A. Theißen, R. Drenckhahn, and H. Buchner, "Improving source reconstructions by combining bioelectric and biomagnetic data," *Electroencephalogr. Clin. Neurophysiol.*, vol. 107, pp. 93–111, 1998.
- [34] G. Anogianakis, J. M. Badier, G. Barrett, S. Erné, R. Fenici, P. Fenwick, F. Grandori, R. Hari, R. Ilmoniemi, F. Mauguère, D. Lehmann, F. Perrin, M. Peters, G.-L. Romani, and P. M. Rossini, "A consensus on relative merits of EEG and MEG," *Electroencephalogr. Clin. Neurophysiol.*, vol. 82, pp. 317–319, 1992.



**Sónia I. Gonçalves** was born in Lisbon, Portugal, in 1973. She received the M.Sc. degree in physics from the Technical University of Lisbon, Portugal, in 1996 and the Ph.D. degree in biophysics from the University of Lisbon, Portugal, in 2002.

She is currently a Postdoctoral Fellow in the MEG Centre—VUMC Vrije Universiteit Medical Centre, Amsterdam, The Netherlands, on leave from the Institute of Biophysics and Biomedical Engineering, University of Lisbon, Portugal. Her research interests include the forward and inverse

problems in EEG, MEG, and EIT. In addition, she is also currently interested in processing EEG and fMRI data, recorded simultaneously.



**Jan C. de Munck** was born in 1962. He received the M.Sc. degree in experimental physics (*cum laude*) and the Ph.D. degree (*cum laude*) from the University of Amsterdam, The Netherlands, in 1985 and 1989, respectively.

His research interest is in forward and inverse modeling applied in medicine (EEG–MEG–EIT) and functional brain imaging (PET–fMRI–MEG). Currently, he is a Staff Member at the University Hospital Vrije Universiteit, Amsterdam, The Netherlands.



**Jeroen P. A. Verbunt** was born in Eindhoven, The Netherlands, in 1971. He received the M.Sc. degree in applied physics at the Eindhoven University of Technology, The Netherlands.

He is now a Staff Member at the MEG center of the VU University Medical Center, Amsterdam, The Netherlands, and is in training for medical physicist.



**Fetsje Bijma** was born in 1977. She received the M.Sc. degree in pure mathematics (*cum laude*) from the RijksUniversiteit Groningen, Groningen, The Netherlands, in 2000. She is currently working toward the Ph.D. degree at the Vrije Universiteit Medical Center, Amsterdam, The Netherlands.

Her research interests include the inverse modeling and statistical analysis of MEG and EEG data.



**Rob M. Heethaar** received the M. Sc. degree in physics and mathematics and the Ph.D. degree from Utrecht University, Utrecht, The Netherlands, in 1969 and 1972, respectively.

From 1969 to 1985, he held joint appointments at the Departments of Cardiology and Medical Physics at Utrecht University. His main interest is physics of the heart and circulation. From 1972 to 1974, he worked on artificial electrical stimulation of the heart. He spent the next two years at the Mayo Clinic working in the field of cardiac mechanics. In

1981, he became Professor of Bio-Engineering at the University of Technology Twente, The Netherlands, and, in 1987, Professor of Medical Physics at Utrecht University, Utrecht, The Netherlands. He founded two Dutch companies in bio-engineering. Since 1993, he has been a Professor of Medical Physics and Informatics and Chairman of the department at the Vrije Universiteit, Amsterdam, The Netherlands. He is the author of numerous papers on electrophysiology, cardiac mechanics, bio-engineering, and hemorheology, and he is referee of several scientific journals. His current main topics of research are related to the development of bio-impedance and MRI tagging techniques to assess cardiac pumpfunction noninvasively.

Dr. Heethaar has received several awards for his contributions to science.



**Fernando Lopes da Silva** received the M.D. degree from the University of Lisbon, Lisbon, Portugal, in 1959. He received the Ph.D. degree from the University of Utrecht, Utrecht, The Netherlands, in 1970. He received the Doctor Honoris Causa degree from the University of Lisbon, in 1997 and from the University of Porto, Porto, Portugal, in 2002.

He was awarded a Gulbenkian Scholarship (1962–1964) to follow a postgraduate course on engineering and physics for physiologists at the Imperial College of the University of London,

London, U.K., and to work at the Department of Physiology and Pharmacology of the National Institute of Medical Research (Mill Hill). Thereafter, he went to Utrecht, The Netherlands, to work with S. van Leeuwen of the Institute of Medical Physics (TNO). There he started his Ph.D. research work on system analysis of visual evoked potentials. In 1973, he followed S. van Leeuwen as the head of the Brain Research Group, University of Utrecht, The Netherlands. In 1975, he became Deputy Director of the Institute of Medical Physics TNO where he was in charge of the scientific research work. He was appointed Full Professor in General Animal Physiology at the Faculty of Sciences at the University of Amsterdam in 1980. From 1975 to 1985, he taught neurophysiology as a Visiting Professor at the Twente University (THT, Enschede) as part of the Biomedical Engineering program. In 1993, he was appointed Scientific Director of the newly created Institute of Neurobiology, and member of the Scientific Directorate of the Graduate School of Neurosciences Amsterdam. From 1995 to 2002, he was Scientific Director of the Institute for Epilepsy “Meer en Bosch” in Heemstede. In September 2000, he became Emeritus Professor of the University of Amsterdam. His research interests are mainly the study of the basic electrophysiology of the central nervous system, including the biophysical aspects of electrical activity in the brain (EEG/MEG) and the functional organization of neural networks in relation to cognitive functions. Furthermore, his current research interests are directed to the questions of the functions of the limbic structures and of the origin of epileptic phenomena.

Dr. Lopes da Silva was elected member of the Netherlands Royal Academy of Arts and Sciences in 1985. In 1999, he received the Herbert H. Jasper Award from the American Clinical Neurophysiology Society. In August 2000, he was elected an Honorary Member of the Dutch Society of Clinical Neurophysiology. In 2000, he was awarded the degree of grand-officer of the Order of Santiago da Espada by the President of the Republic of Portugal, and, in 2001, he was awarded the degree of Knight of the Order of the Nederlandse Leeuw by the Queen of the Netherlands, in appreciation for his achievements in science.